Supplemental Material for: Ultrafast Photo-Induced Phonon Hardening Due to Pauli Blocking in $MAPbI_3$ Single-Crystal and Polycrystalline Perovskites

Chelsea Q. Xia[1], Samuel Poncé[2,3], Jiali Peng[4], Aleksander M. Ulatowski[1], Jay B. Patel[1], Adam D. Wright[1], Rebecca L. Milot[5], Hans Kraus[6], Qianqian Lin[4], Laura M. Herz[1,7], Feliciano Giustino[2,8,9] and Michael B. Johnston[1,*]

[1]*Department of Physics, University of Oxford, Clarendon Laboratory, Parks Road, Oxford OX1 3PU, U.K.*

[2]*Department of Materials, University of Oxford, Parks Road, Oxford OX1 3PH, U.K.*

[3]*Theory and Simulation of Materials (THEOS), École Polytechnique Fédérale de Lausanne, CH-1015 Lausanne, Switzerland*

[4]*Key Lab of Artificial Micro- and Nano-Structures of Ministry of Education of China, School of Physics and Technology, Wuhan University, Wuhan 430072, P. R. China*

[5]*Department of Physics, University of Warwick, Gibbet Hill Road, Coventry CV4 7AL, U.K.*

[6]*Department of Physics, University of Oxford, Denys Wilkinson Building, Keble Road, Oxford OX1 3RH, U.K.*

[7]*TUM Institute for Advanced Study, 85748 Garching bei München, Germany*

[8]*Oden Institute for Computational Engineering and Sciences, The University of Texas at Austin, Austin, Texas 78712, USA*

[9]*Department of Physics, The University of Texas at Austin, Austin, Texas 78712, USA*

[*] E-mail: michael.johnston@physics.ox.ac.uk

Contents

1 Terahertz spectroscopy

Supplementary Figure 1 demonstrates the experimental setup of the THz time-domain spectroscopy (THz-TDS) and optical-pump-THz-probe spectroscopy (OPTPS) in transmission and reflection geometries. An amplified laser with central wavelength of 800 nm, 5 kHz repetition rate, 35 fs pulse width and 4 W average power is split into three arms: gate beam, THz beam and pump beam. The THz beam is generated by a spintronic emitter due to inverse spin Hall effect.[1] The pump beam is up-converted to 400 nm by a β-barium-borate (BBO) crystal and a short-pass filter is used to filter out the residual 800 nm light. The resultant THz signal is detected by electro-optic sampling using a set of a (110) ZnTe crystal, a quarter-wave plate, a Wollaston prism and a pair of balanced photodiodes. A silicon beamsplitter is used to direct the reflected THz signal from the sample to another detection arm. The temperature of the sample is changed by a cold-finger cryostat (Oxford Instruments, MicrostatHe). The photoluminescence (PL) spectrum of the sample generated by the pump beam is collected by a fibre-coupled spectrometer (Horiba Scientic, iHR320).

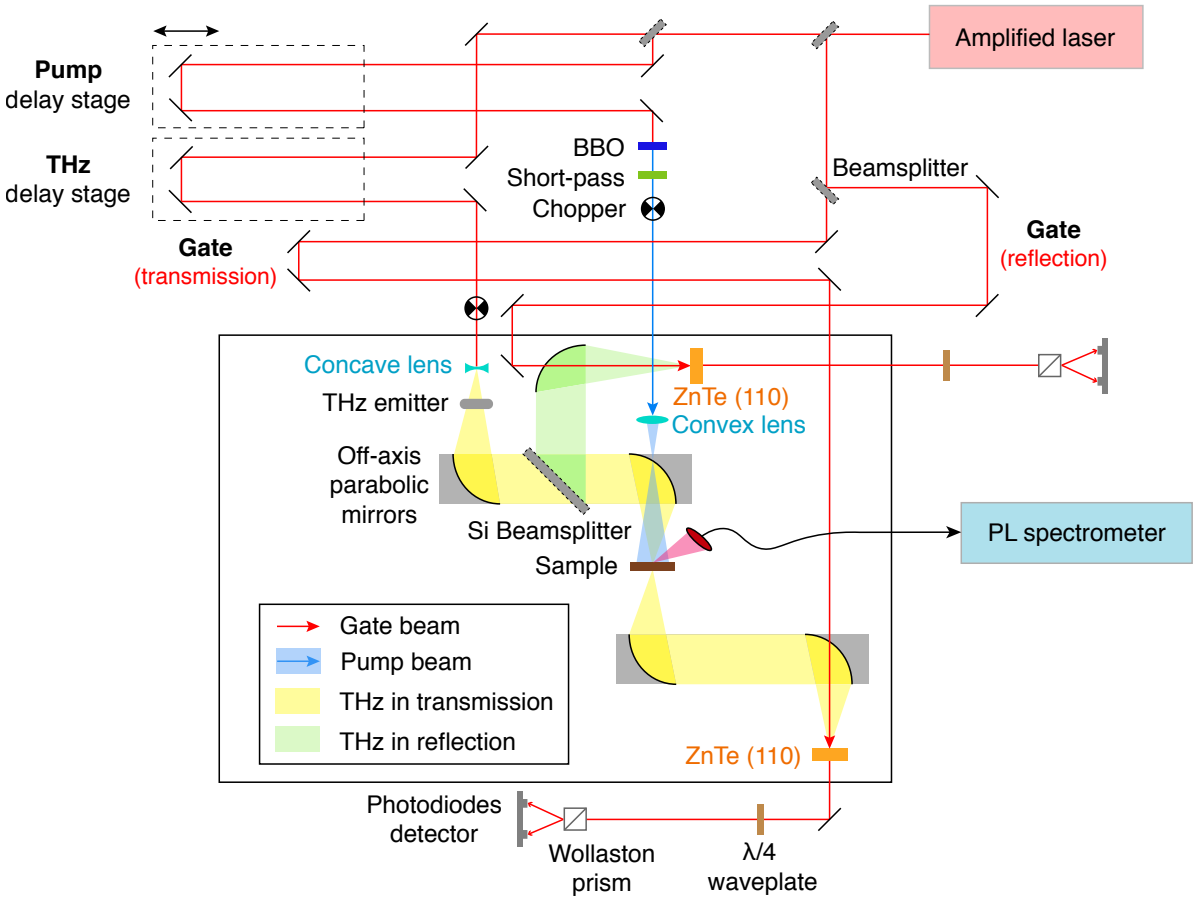

Supplementary Figure 1: Schematic of THz-TDS and OPTPS setup in transmission and reflection geometries.

2 Derivation of absorption and photoconductivity

2.1 Analysis of THz reflection measurements

Since the $MAPbI_3$ single crystal is so thick that the THz signal can only be measured in reflection, its phonon modes have to be analysed in terms of the absorption spectrum which is obtained by extracting the dielectric function ε from its reflectivity r:

$$r(\omega) = \left| \frac{1 - \sqrt{\varepsilon(\omega)}}{1 + \sqrt{\varepsilon(\omega)}} \right|^2 . \tag{S1}$$

The Kramers-Kronig (KK) transformation is applied according to the dynamical coupling between the real part $\varepsilon_1(\omega)$ and the imaginary part $\varepsilon_2(\omega)$ of the dielectric function. Explicitly, this non-independent relationship is governed by the following equations:[2,3]

$$\varepsilon_1(\omega) = \frac{2}{\pi} \mathcal{P} \int_0^\infty \frac{x \varepsilon_2(x)}{x^2 - \omega^2} dx + 1, \tag{S2}$$

$$\varepsilon_2(\omega) = -\frac{2\omega}{\pi} \mathcal{P} \int_0^\infty \frac{\varepsilon_1(x)}{x^2 - \omega^2} dx + \frac{4\pi\sigma_{\mathrm{DC}}}{\omega}, \tag{S3}$$

where σ_{DC} is the DC conductivity and $\mathcal{P}$ is the principal value integral. Combining Equations (S1)–(S3), we can extract the complex dielectric function from the experimentally measured reflectivity spectrum.

Here, we utilise the method of variational dielectric functions (VDF) which is a combination of two approaches.[4] On one hand, we use the technique of least squares fitting to fit the reflectivity spectrum, $r(\omega)$, with as many Lorentzian oscillators as the number of data points which essentially compose the imaginary part of the dielectric function. On the other hand, we use the KK transformation to restore the corresponding real part of the dielectric function. Consequently, the full spectral information of the material can be obtained from this KK-constrained variational fitting method. This method has the ability to fit any reflectivity

spectrum as long as enough Lorentzian oscillators are included, thanks to the completeness of Drude-Lorentz functions. In another word, any physical dielectric function can be approximated by a sum of Lorentzian oscillators. The VDF method is a numerical method which extracts the dielectric function from the reflectivity spectrum numerically with no analytical expression. Therefore, there can be indefinitely many flexible parameters, depending on the number of Lorentzian oscillators that are used to fit the reflectivity spectrum. However, this huge flexibility of the fitting parameters may cause some uncontrollable divergence in the fitting process. To avoid this problem, we fix some of the parameters in a certain way. Specifically, the frequency of each Lorentzian oscillator is equally spaced over the entire frequency range of the reflectivity measurement and the scattering rate (line width) of each oscillator is also fixed. In our study of $MAPbI_3$ perovskite, we set $\omega_1 = \omega_{\min}$, $\omega_N = \omega_{\max}$ and $\omega_{i+1} - \omega_{i-1} = \gamma_i$.[4] Furthermore, the VDF method is applicable in a wide frequency range not only limited in THz range. For instance, we can apply the same analysis to the reflectivity spectrum obtained from Fourier-transform infrared spectroscopy (FTIR) which covers the optical range. We use a program called RefFIT which is based on VDF to fit the reflectivity spectrum of the $MAPbI_3$ single crystal.[5]

Knowing the complex dielectric function, we can also obtain other optical properties of the material, such as the complex refractive index $\tilde{n}(\omega)$:

$$\tilde{n}(\omega) = n(\omega) + \mathrm{i}\kappa(\omega) = \sqrt{\varepsilon(\omega)}, \tag{S4}$$

where the imaginary part $\kappa(\omega)$ is known as the extinction coefficient and is directly related to the absorption coefficient $\alpha(\omega)$ according to the following equation[6]

$$\alpha(\omega) = \frac{4\pi\kappa(\omega)}{\lambda} = \frac{2\omega\kappa(\omega)}{c}. \tag{S5}$$

In the case of $MAPbI_3$ thin film, the extraction of absorption is more straightforward,

since the dielectric function can be calculated directly from the conductivity,[7]

$$\varepsilon(\omega) = \varepsilon_\infty + \frac{\mathrm{i}}{\varepsilon_0 \omega}\sigma(\omega), \tag{S6}$$

where ε_∞ is the dielectric constant of $MAPbI_3$ at high frequency and ε_0 is the permittivity of free space. The absorption spectrum is obtained by combining Equations (S4) and (S5).

For a single phonon mode the complex dielectric function can be fitted by a Lorentzian oscillator,[7]

$$\varepsilon(\omega) = \varepsilon_\infty + (\varepsilon_{\mathrm{stat}} - \varepsilon_\infty)\frac{\omega_{\mathrm{TO}}^2}{\omega_{\mathrm{TO}}^2 - \omega^2 - \mathrm{i}\gamma_{\mathrm{TO}}\omega}, \tag{S7}$$

where $\varepsilon_{\mathrm{stat}}$ is the static dielectric constant of $MAPbI_3$, ω_{TO} is the TO phonon frequency and γ_{TO} is the phonon scattering rate.

Generalising for N TO phonons the dieletric function becomes,

$$\varepsilon(\omega) = \varepsilon_\infty + \sum_j^N \frac{f_j\, \omega_{\mathrm{TO},j}^2}{\omega_{\mathrm{TO},j}^2 - \omega^2 - \mathrm{i}\gamma_{\mathrm{TO},j}\omega}, \tag{S8}$$

where $\omega_{\mathrm{TO},j}$ is the frequency of the jth TO phonon mode, f_j is its oscillator strength, which in Equation (S7) is given by the difference between the low and high frequency dielectric constants, i.e. $f = (\varepsilon_{\mathrm{stat}} - \varepsilon_\infty)$. $\gamma_{\mathrm{TO},j}$ is the corresponding phonon scattering rate. Combining Equations (S6) and (S8) gives the expression given in Equation (3) of the main text. A least squares fitting algorithm was used to fit that equation to the experimental data in Figure 2 of the main text.

On the other hand, when photoexcitation is applied, the change in THz reflection is proportional to the photoconductivity as mentioned in the main text. The analytic expression for the photoconductivity measured in reflection is derived by solving the wave equation,[8]

$$\frac{d^2\Delta E(z)}{dz^2} + k^2 \Delta E = -\mathrm{i}k_0 Z_0 \Delta j(z), \tag{S9}$$

where ΔE is the change of THz electric field due to photoexcitation, z is the distance along

which the THz pulse propagates, k is the wave vector of the THz field in the sample and k_0 is the wave vector in vacuum. Z_0 is the vacuum wave impedance and $\Delta j(z) = \Delta\sigma(z)E(z)$ represents the current density where $\Delta\sigma(z)$ is the photoconductivity arising from free charge carriers.

In the reflection measurement, the ratio between change of reflectivity, ΔR and the non-photoexcited reflectivity, R, is expressed as,

$$\frac{\Delta R}{R} = \frac{\Delta E_r}{E_r} = \frac{E_e - E_0}{E_0} \tag{S10}$$

where E_e and E_0 represent the THz field under photoexcitation and without photoexcitation respectively. Using the continuity conditions of the electric and magnetic fields to solve Equation (S9), ΔE_r is given by,

$$\Delta E_r = -\frac{Z_0 t_1^2 a^2}{2n_1}\Bigg[\int_0^L \exp(2\mathrm{i}kz)\Delta\sigma(z)dz + 2r_2\exp(2\mathrm{i}kL)\int_0^L \Delta\sigma(z)dz + [r_2\exp(2\mathrm{i}kL)]^2\int_0^L \exp(-2\mathrm{i}kz)\Delta\sigma(z)dz\Bigg], \tag{S11}$$

where $t_1 = 2n_1/(n_0 + n_1)$ is the transmission coefficient at the front sample surface with n_0 and n_1 representing the refractive indices of the sample and the surrounding medium ($n_1 = 1$ for air) at THz frequencies respectively. a parameterizes the internal reflections and is equal to 1 in the case of single crystal. r_2 represents the reflection coefficient at the back surface of the single crystal, which is neglected. As a result, Equation (S11) is simplified as,

$$\frac{\Delta R}{R} = \frac{2Z_0}{n_0^2 - n_1^2}\int_0^L \exp(\mathrm{i}2n_0\omega z/c)\Delta\sigma(z)dz. \tag{S12}$$

Assuming the photoconductivity follows the Lambert-Beer law (which is a reasonable assumption for optical excitation of free charge carriers), $\Delta\sigma(z) = \Delta\sigma_s\exp(-\alpha z)$, where α is the absorption coefficient of the sample at optical wavelengths and $\Delta\sigma_s$ is the surface

photoconductivity, Equation (S12) results in,

$$\frac{\Delta R}{R} = \frac{2Z_0}{n_0^2 - n_1^2} \frac{\Delta\sigma_s}{\alpha} \frac{1}{1 - \frac{2i\omega n_0}{\alpha c}}, \tag{S13}$$

and rearranging for $\Delta\sigma_s$ leads to Equation (6) given in the main text.

2.2 Photoconductivity correction of $MAPbI_3$ thin films

Conventionally, the THz photoconductivity measured in transmission is expressed by the following equation,

$$\Delta\sigma(\omega) = -\frac{\varepsilon_0 c(1+\tilde{n_s})}{d}\left(\frac{\Delta T}{T_{\text{off}}}\right), \tag{S14}$$

from which some "phonon-modulation" features superimposed on top of the Drude response is attributed to electron-phonon coupling effect.[9,10] However, recent studies have shown that those phonon modulations could be removed by separating the effect of phonon modes observed in the dark conductivity from the measured photoconductivity spectrum. Consequently, a more accurate expression for the photoconductivity is written as,[11,12]

$$\Delta\sigma(\omega) = -\frac{\varepsilon_0 c(1+\tilde{n_{\text{s}}})}{d}\left(\frac{\Delta T}{T_{\text{on}}}\right)\left(\frac{T_{\text{reference}}}{T_{\text{off}}}\right). \tag{S15}$$

Using this equation, the phonon modulation of the Drude response observed in the photoconductivity of $MAPbI_3$ thin film measured at room tempearture may be removed. As demonstrated in Supplementary Figure 2a, the photoconductivity calculated using Equation (S14) where the effect of dark conductivity is not corrected (blue dots), shows two phonon modulation peaks at 1 and 2 THz. In contrast, when the dark conductivity correction is applied via Equation (S15) which is represented by the red triangles, the photoconductivity shows a pure Drude response. This suggests that electron–phonon coupling is negligible in the $MAPbI_3$ thin film at room temperature, as opposed to previously reported strong coupling effect.[13] However, in the case of low temperature (Supplementary Figure 2b)

where the photoconductivity of the thin film was measured at 5 K, even after the correction, the phonon modulations still persist in the Drude response, although the strength of the corrected modulation (red triangles) is slightly weaker than before when no correction is applied (blue dots). Therefore, we conclude that the electron–phonon coupling effect is still existent in $MAPbI_3$ perovskite, although at room temperature it might not be as noticeable as that at low temperatures. This analysis suggests that when analysing the photoconductivity spectrum of $MAPbI_3$, it is critical to take into account the effect of phonon modes and failure to separate the phonon modulation from the photoconductivity spectrum may lead to misinterpretation of electron-phonon coupling.

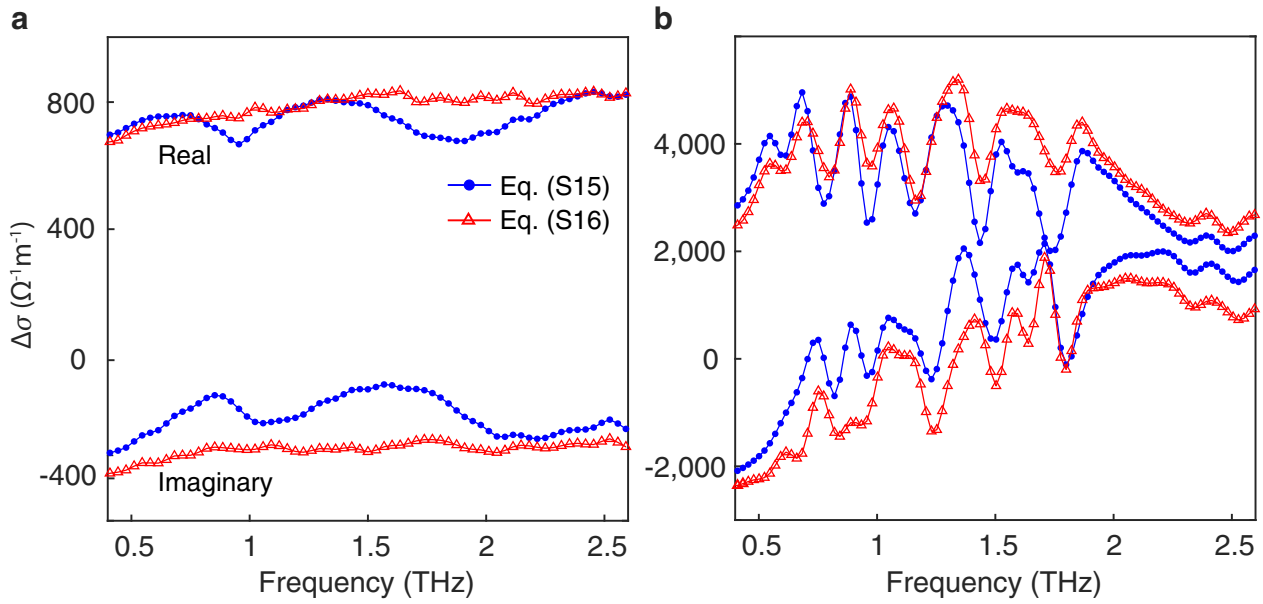

Supplementary Figure 2: Photoconductivity of $MAPbI_3$ thin film measured at 5 ps after photoexcitation at (a) 295 K and (b) 5 K. The blue dots and the red triagnles represent the photoconductivity calculated using Equation (3) and Equation (4) respectively given in the main text.

To confirm the consistency between the transmission and reflection measurements, Supplementary Figure 3 shows the photoconductivity spectra of $MAPbI_3$ thin film measured in transmission and reflection. Without the spectra correction given by Equation (S15), both spectra show phonon-modulation peaks at 1 THz and 2 THz. While the transmitted photoconductivity spectra can be corrected by Equation (S15) as demonstrated in Supplementary

Figure 2, the correction of the reflection spectra is complicated and requires more detailed analysis. Nevertheless, by comparing the raw photoconductivity data, $-\Delta T/T$ and $-\Delta R/R$, it is clear that the results obtained by the transmission and reflection measurements are consistent. Therefore, it is reliable to measure the photoconductivity spectra of $MAPbI_3$ single crystal in reflection only, even though the transmission measurement is not achievable.

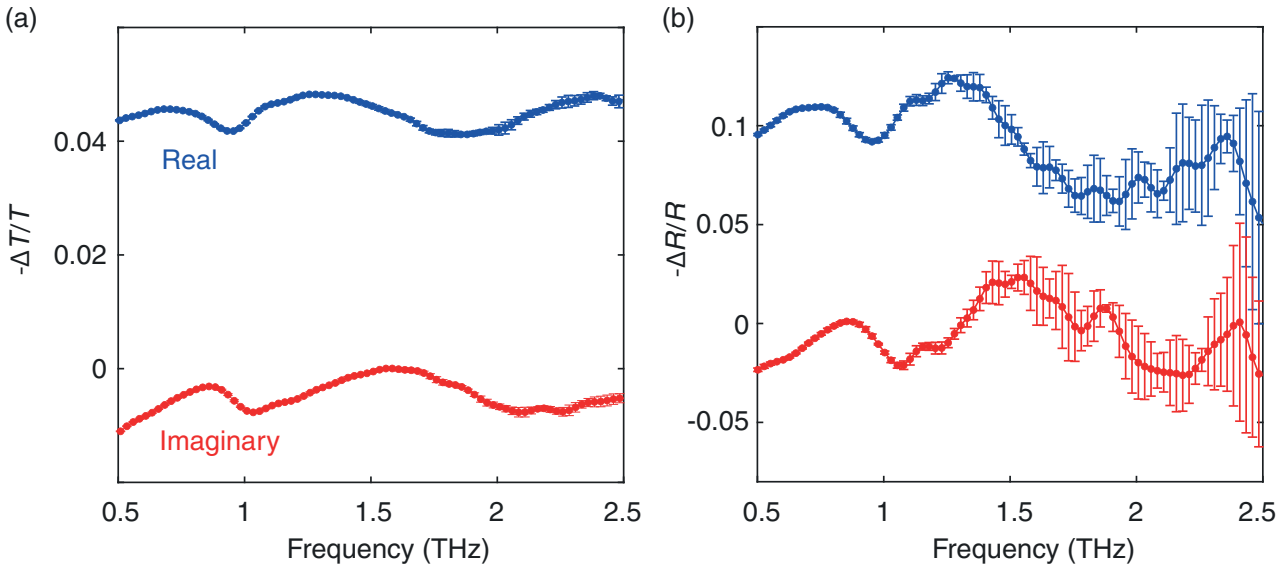

Supplementary Figure 3: Photoconductivity of $MAPbI_3$ thin films measured in (a) transmission and (b) reflection at 5 ps after photoexcitation at 295 K. The blue circles and red circles represent the real and imaginary parts of the photoconductivity respectively.

Apart from photoconductivity measurement, OPTPS can also be used for measuring transient THz absorption spectra as a function of photoexcitation fluence, from which the charge-carrier mobility can be extracted. The fluence-dependent transient THz absorption spectra of $MAPbI_3$ thin film and single crystal were published in Ref. 14, where the single crystal was found to have a higher mobility than the thin film.

3 Temperature dependence of phonon lifetimes

In a completely harmonic crystal the phonon lifetimes are infinite and the phonons have a frequency independence of temperature.[15] Thus one measure of anhamonicity is the phonon lifetime. Supplementary Figure 4 shows the phonon lifetime versus temperature for single-crystal $MAPbI_3$ (blue) compared with polycrystalline thin-film $MAPbI_3$ for mode (3) as listed in Table 1 of the main text. It can be seen the the phonon lifetime is considerably longer for the single crystal. For comparison the optical phonon lifetime for GaAs is 3.5 ps at 300 K and 7ps at 77 K.[16,17]

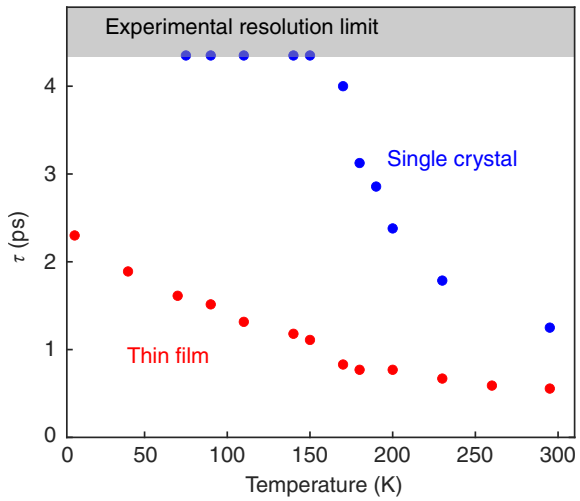

Supplementary Figure 4: Phonon lifetime as a function of lattive temperature for a $MAPbI_3$ single crystal (blue) and a thin film (red). Phonon lifetimes were extracted from the experimental data for mode (3) shown in Figure 1 of the main text. The shaded region shows the maximum lifetime measureable with the experiment owing to its limited spectra resolution.

4 Temperature dependence of bandgap

As mentioned in the main text, the bandgap of the $MAPbI_3$ thin film and single crystal opens with increasing temperature, whose rate is different between the orthorhombic and the tetragonal phases. To demonstrate this more clearly, Supplementary Figure 4 shows the PL peak energy of the $MAPbI_3$ single crystal and thin film, which is a rough estimate of their bandgap energy, as a function of temperature. The PL spectrum at each temperature was fit with a two-Gaussian function, from which the central wavelength of the dominant peak was converted to energy and plotted in Supplementary Figure 5 (details of the two-Gaussian fit are reported in Ref. 14). It should be noted that the PL peak energy slightly underestimates the bandgap energy, whereas a more accurate determination of the bandgap energy can be achieved by the Elliot fit on the absorption bandgap.[18] Nevertheless, Supplementary Figure 5 shows that above the phase transition temperature ($\sim 150\,\mathrm{K}$), the bandgap decreases abruptly and the bandgap opening rate drops from $0.46\,\mathrm{meV\,K^{-1}}$ to $0.33\,\mathrm{meV\,K^{-1}}$.

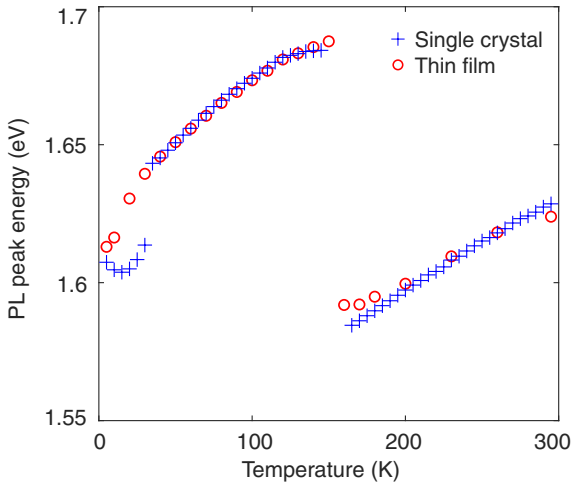

Supplementary Figure 5: PL peak energy of the $MAPbI_3$ single crystal (blue crosses) and the thin film (red circles) as a function of temperature. According to Ref. 18, the true bandgap energy is expected to be 26 meV and 15 meV larger in the orthorhombic and tetragonal phases respectively.

5 Photo-induced blueshift of phonon modes

In order to demonstrate the phonon-shift phenomenon in $MAPbI_3$ more clearly, we compare the conductivity (and reflectivity) spectra measured on samples with and without photoexcitation separately. As shown in Supplementary Figure 6(c), a clear blueshift of phonon frequency is observed in the reflectivity spectrum of $MAPbI_3$ single crystal measured at 75 K, which is indicated by the black arrows. However, in contrast, the blueshift of phonon frequency in the case of $MAPbI_3$ thin film (Supplementary Figure 6a and 6b) is much less noticeable, owing to the much broader phonon peaks associated with the polycrystalline samples.

Furthermore, the blueshift in single crystal measured at 295 K (Supplementary Figure 6d) becomes less obvious due to the effect of phonon broadening, which makes the shifted phonon peak less-well resolved and hence less prominent. Meanwhile, no blueshift is observed in the thin film at 295 K, owing to the shorter-lived phonon modes. On the other hand, the more persistent phonon-hardening effect observed in the $MAPbI_3$ single crystal suggests that the longer phonon lifetimes may contribute to prolonging the phonon-hardening process. One consequence of this phenomenon is that although the single crystal has the advantage of having no grain boundaries to achieve higher electrical mobility, its longer-lived phonons can suppress the mobility more significantly compared to the thin film, which places an upper limit to the photovoltaic performance of single-crystal-based devices.

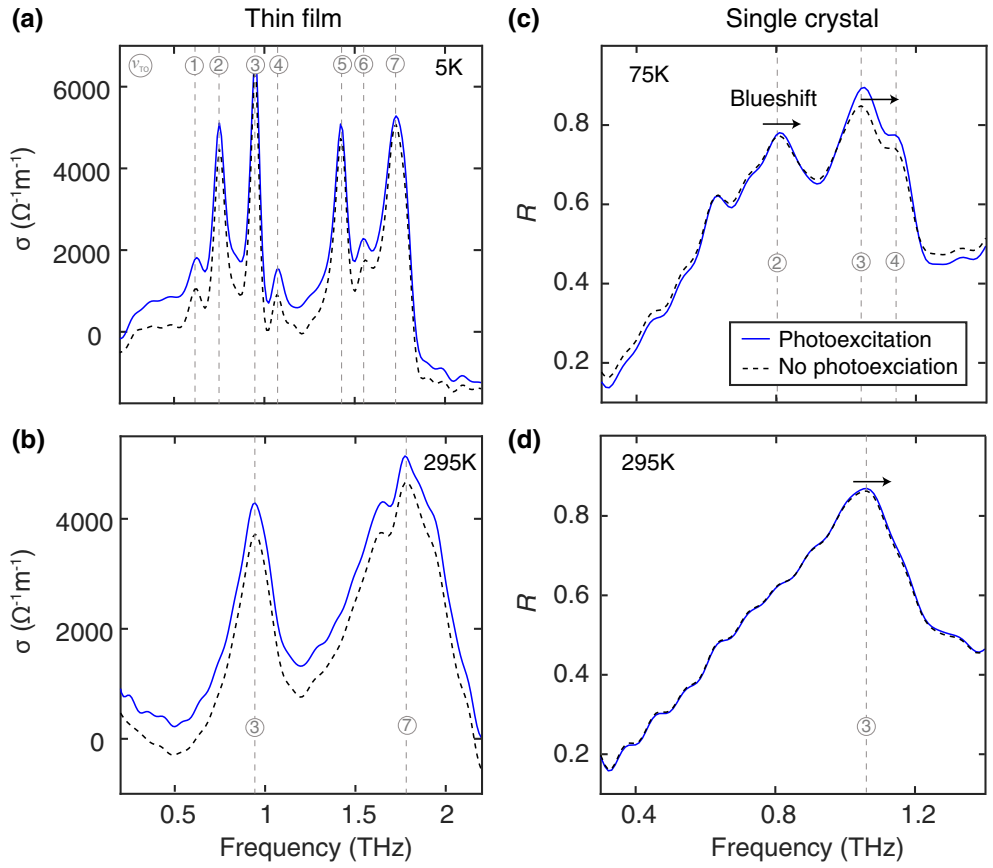

Supplementary Figure 6: Conductivity spectra of $MAPbI_3$ thin film measured at (a) 5 K and (b) 295 K. Reflectivity spectrum of $MAPbI_3$ single crystal measured at (c) 75 K and (d) 295 K. The blue curves represent the measurements taken without photoexcitation and the red curves represent the measurements taken at 5 ps after photoexcitation under fluence 48 μJcm^{-2}.

6 First-principles calculations of cubic $CsPbI_3$

Using self-consistent many-body correction, we computed the bandgap of $CsPbI_3$ to be 0.86 eV with a 0.16 and 0.17 hole and electron effective masses locate at the R-point[19] and show the electronic band structure in Supplementary Figure 7. We computed the adiabatic phonon band structure of $CsPbI_3$ in Supplementary Figure 8 and observed soft modes which relate to the octahedral tilting instability in the cubic phase and are stabilized by anharmonic effects.[20] Indeed, it is experimentally found that the iodine atoms rapidly fluctuates around their equilibrium positions.[21] Simulating this effect *ab-initio* would requires many atomic configurations weighted by their thermodynamical probability for a given temperature and has never been done so far due to its prohibitive computational cost. Nevertheless, to assess the importance of the soft modes contribution in cubic $CsPbI_3$ on the electron-phonon properties, we repeated the calculations by setting the energy of the soft modes to $\hbar\omega$=1 meV and obtained almost identical results,[19] indicating a negligible contribution of those modes to the overall electron-phonon coupling.

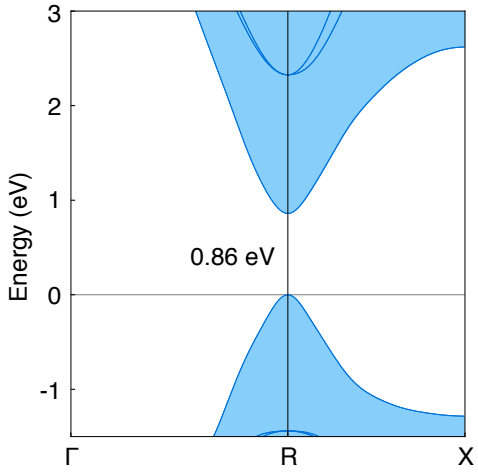

Supplementary Figure 7: Electronic band structure of $CsPbI_3$ using a = 6.276 Å lattice parameter.

We used a rigid band approximation to simulate doping and compute that the Fermi level will be located 7.8 meV, 35.0 meV and 155.2 meV below the valence band maximum for

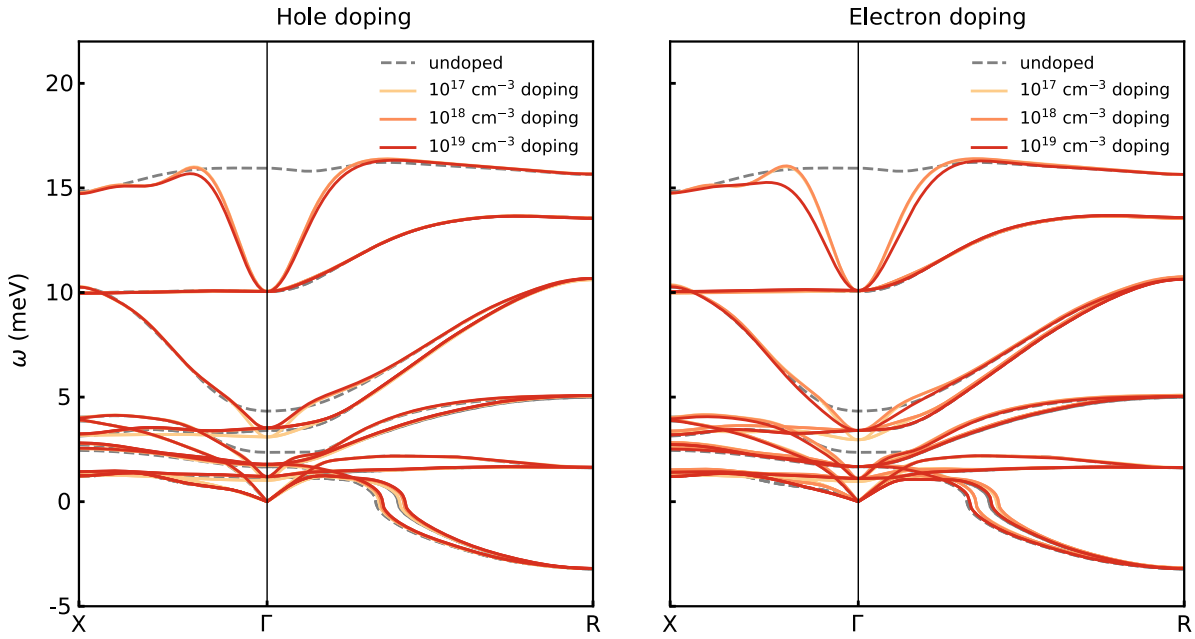

Supplementary Figure 8: Adiabatic phonon bandstructure with doping of $CsPbI_3$ using $a = 6.276$ Å lattice parameter. The highest TO phonon mode frequency (which is the measured one) increases by 0.1698 cm^{-1}, 0.0522 cm^{-1}, and -0.0089 cm^{-1} for 10^{17}, 10^{18} and 10^{19} cm^{-3} hole doping, respectively; and by 0.3176 cm^{-1}, 0.2313 cm^{-1}, and 0.436 cm^{-1} for 10^{17}, 10^{18}, and 10^{19} cm^{-3} electron doping, respectively.

10^{17}, 10^{18}, and 10^{19} cm^{-3} hole doping, respectively. If instead we computed electron doping, we find the Fermi level to be 6.6 meV, 33.8 meV, and 138.1 meV above the conduction band minimum for 10^{17}, 10^{18}, and 10^{19} cm^{-3} electron doping, respectively. Such doping screens the electrons leading to a total suppression of the LO-TO splitting from the phonon band structure as shown in Supplementary Figure 8. This suppression dip has a size proportional to two times the Fermi wavevector and therefore increases with doping. In our experiment, normal probing allows us only to excite transverse phonon frequency (TO modes). We can see in Supplementary Figure 8 that the effect of adiabatic doping is to increase the highest TO phonon frequency (we sum the hole and electron doping contribution to the shift) by 0.4874 cm^{-1}, 0.2835 cm^{-1}, 0.4271 cm^{-1} for 10^{17}, 10^{18}, and 10^{19} cm^{-3}, respectively.

Those adiabatic effects are temperature independent. To include temperature effects, we

compute the non-adiabatic phonon self-energy as:[22]

$$\Pi^{\mathrm{NA}}_{\mathbf{q}\nu}(\omega,T)=\sum_{mn}\int_{\mathrm{BZ}}\frac{d\mathbf{k}}{\Omega_{\mathrm{BZ}}}g^{b}_{mn\nu}(\mathbf{k},\mathbf{q})g_{mn\nu}(\mathbf{k},\mathbf{q})\left(\frac{f_{n\mathbf{k}}-f_{m\mathbf{k}+\mathbf{q}}}{\varepsilon_{m\mathbf{k}+\mathbf{q}}-\varepsilon_{n\mathbf{k}}-(\omega+i\delta)}-\frac{f_{n\mathbf{k}}-f_{m\mathbf{k}+\mathbf{q}}}{\varepsilon_{m\mathbf{k}+\mathbf{q}}-\varepsilon_{n\mathbf{k}}-i\delta}\right), \tag{S16}$$

where $g_{mn\nu}(\mathbf{k},\mathbf{q})$ is the matrix element for the scattering of an electron from the initial state $|n\mathbf{k}\rangle$ to the final state $|m\mathbf{k}+\mathbf{q}\rangle$ via a phonon of branch ν, wavevector $\mathbf{q}$, and frequency $\omega_{\mathbf{q}\nu}$. The sum is over the first Brillouin zone Ω_{BZ} where the electronic states have energy $\varepsilon_{n\mathbf{k}}$, band index n and wavevector $\mathbf{k}$ and where $f_{n\mathbf{k}}$ is the Fermi-Dirac function. The temperature only enters in Equation (S16) via the f distribution function. The δ in Equation (S16) is linked with the electronic lifetime which was computed in prior works[19,23] to be 3 meV and 31 meV at 30 K and 300 K, respectively. Finally the $g^{b}_{mn\nu}(\mathbf{k},\mathbf{q})=g_{mn\nu}(\mathbf{k},\mathbf{q})\epsilon(q)$ is the bare electron-phonon interaction and has been obtained by unscreening the $g_{mn\nu}(\mathbf{k},\mathbf{q})$ with the Thomas-Fermi model dielectric function of Ref. 24:

$$\epsilon(q)=\frac{k_0^2+q^2}{k_0^2\sin(qR)/(qR\,\epsilon_0)+q^2}, \tag{S17}$$

where $q=|\mathbf{q}|$, $\epsilon_0=5.9$ is the macroscopic (electronic) dielectric constant. $k_0=1.1134$ are $R=3.9079$ are obtained from the valence electron density ρ as $k_0^2=4(3\pi^2\,\rho)^{1/3}/\pi$ and $\sinh(k_0R)/k_0R=\epsilon_0$.

The phonon line width is obtained by taking the imaginary part of the phonon self-energy:

$$\mathrm{Im}\,\Pi^{\mathrm{NA}}_{\mathbf{q}\nu}(\omega,T)=\pi\sum_{mn}\int_{\mathrm{BZ}}\frac{d\mathbf{k}}{\Omega_{\mathrm{BZ}}}|g_{mn\nu}(\mathbf{k},\mathbf{q})|^2\varepsilon(q)\big(f_{n\mathbf{k}}-f_{m\mathbf{k}+\mathbf{q}}\big)\delta(\varepsilon_{m\mathbf{k}+\mathbf{q}}-\varepsilon_{n\mathbf{k}}-\omega), \tag{S18}$$

whereas the associated spectral function is obtained with:

$$A_{\mathbf{q}}(\omega,T)=\frac{1}{\pi}\sum_{\nu}\frac{2\omega^2_{\mathbf{q}\nu}\,\mathrm{Im}\,\Pi^{\mathrm{NA}}_{\mathbf{q}\nu}(\omega,T)}{(\omega^2-\omega^2_{\mathbf{q}\nu}-2\omega_{\mathbf{q}\nu}\,\mathrm{Re}\,\Pi^{\mathrm{NA}}_{\mathbf{q}\nu}(\omega,T))^2+(2\omega_{\mathbf{q}\nu}\,\mathrm{Im}\,\Pi^{\mathrm{NA}}_{\mathbf{q}\nu}(\omega,T))^2}. \tag{S19}$$

The non-adiabatic renormalized phonon frequency is obtained in the on-the-mass shell ap-

proximation as $\Omega^2_{\mathbf{q}\nu} \approx \omega^2_{\mathbf{q}\nu} + 2\omega_{\mathbf{q}\nu} \operatorname{Re} \Pi^{\mathrm{NA}}_{\mathbf{q}\nu}(\omega_{\mathbf{q}\nu}, T)$. Supplementary Figures 9 and 10 show the non-adiabatic spectral functions of $CsPbI_3$ calculated at 300 K with hole doping densities 10^{18} and $10^{19}\,\mathrm{cm}^{-3}$ respectively. The numerical results are listed in Tables 1–3, where the frequencies of the highest TO phonon and the mid TO modes are calculated under adiabatic and non-adiabatic conditions with doping density ranging from 10^{17} to $10^{19}\,\mathrm{cm}^{-3}$.

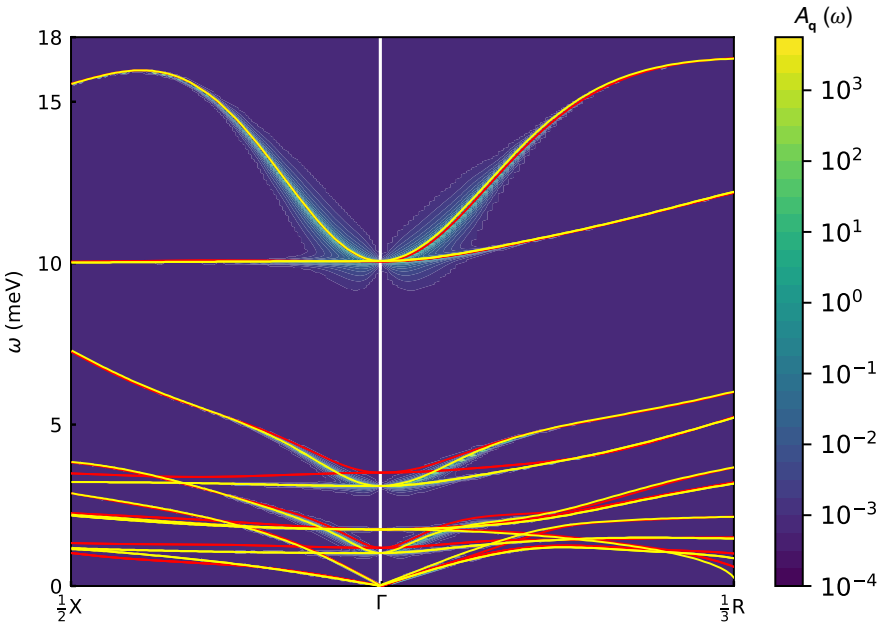

Supplementary Figure 9: Non-adiabatic spectral function with $10^{18}\,\mathrm{cm}^{-3}$ hole doping of $CsPbI_3$ at 300 K using $a = 6.276$ Å lattice parameter. The yellow lines are the non-adiabatic renormalized phonon frequencies $\Omega_{\mathbf{q},\nu}$ and the red lines are the DFPT adiabatic phonon frequencies $\omega_{\mathbf{q},\nu}$.

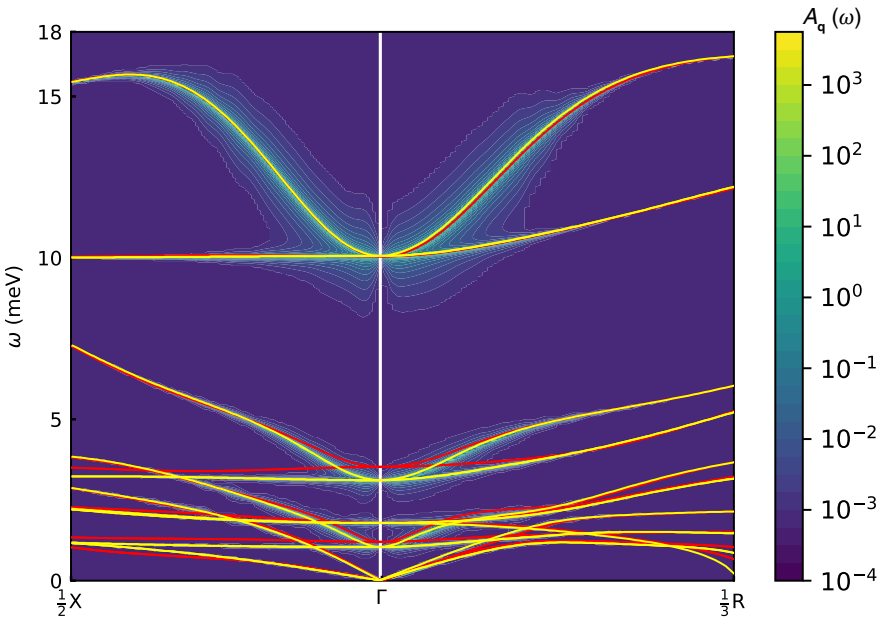

Supplementary Figure 10: Non-adiabatic spectral function with $10^{19}\,\mathrm{cm}^{-3}$ hole doping of $CsPbI_3$ at 300 K using $a = 6.276$ Å lattice parameter. The yellow lines are the non-adiabatic renormalized phonon frequencies $\Omega_{\mathbf{q},\nu}$ and the red lines are the DFPT adiabatic phonon frequencies $\omega_{\mathbf{q},\nu}$.

Supplementary Table 1: Renormalization of the highest TO phonon frequency at the zone center.

	Adiabatic ω_{TO} (cm^{-1})	Non-adiabatic Ω_{TO} (cm^{-1})	
Doping		30 K	300 K
Undoped	81.0186	-	-
Hole 10^{17} cm^{-3}	81.1881	81.1351	81.1353
Hole 10^{18} cm^{-3}	81.0717	-	81.2203
Hole 10^{19} cm^{-3}	81.0106	-	81.1396
Electron 10^{17} cm^{-3}	81.3360	81.2162	81.2164
Electron 10^{18} cm^{-3}	81.2504	-	81.3816
Electron 10^{19} cm^{-3}	81.4556	-	81.5430

Supplementary Table 2: Renormalization of the mid TO (modes 10-11) phonon frequency at the zone center.

	Adiabatic ω_{TO} (cm^{-1})	Non-adiabatic Ω_{TO} (cm^{-1})	
Doping		30 K	300 K
Undoped	27.4562	-	-
Hole 10^{17} cm^{-3}	24.9483	24.8776	24.8777
Hole 10^{18} cm^{-3}	28.3154	-	25.0027
Hole 10^{19} cm^{-3}	28.4328	-	25.0834
Electron 10^{17} cm^{-3}	23.8740	23.8273	23.8275
Electron 10^{18} cm^{-3}	27.4083	-	23.8735
Electron 10^{19} cm^{-3}	27.4509	-	23.9544

Supplementary Table 3: Renormalization of the mid TO (modes 7-8) phonon frequency at the zone center.

	Adiabatic ω_{TO} (cm^{-1})	Non-adiabatic Ω_{TO} (cm^{-1})	
Doping		30 K	300 K
Undoped	13.4219	-	-
Hole 10^{17} cm^{-3}	14.1171	14.0419	14.0419
Hole 10^{18} cm^{-3}	14.1504	-	14.1131
Hole 10^{19} cm^{-3}	14.4238	-	14.4357
Electron 10^{17} cm^{-3}	13.5202	13.4741	13.4742
Electron 10^{18} cm^{-3}	13.5261	-	13.5484
Electron 10^{19} cm^{-3}	13.5436	-	13.5485

We approximate the experimental photoexcitation as the sum of hole and electron doping. This amounts to neglect electron-hole interactions. We therefore compute a phonon hardening of highest TO mode of 0.3145 cm^{-1}, 0.5647 cm^{-1} and 0.6446 cm^{-1} at 10^{17} cm^{-3}, 10^{18} cm^{-3}, and 10^{19} cm^{-3} doping respectively, which is detailed in Table 2 of the main text. We found that most of the effect comes from the adiabatic doping and that non-adiabatic and temperature effects are small in comparison. The main effect comes from the massive increase in dielectric screening resulting from the doping and seems to depend only weakly on doping concentration at higher doping.

Finally, we looked at the effect of lattice contraction with doping and found out that the relaxed lattice parameter contracts from 6.3812 Å to 6.3628 Å with 10^{19} cm^{-3} doping yielding a phonon hardening of the highest TO mode by 3.6 cm^{-1}. However a global lattice contraction upon excitation is expected to happen on a longer timescale than the one investigated here.

References

(1) Seifert, T.; Jaiswal, S.; Sajadi, M.; Jakob, G.; Winnerl, S.; Wolf, M.; Kläui, M.; Kampfrath, T. Ultrabroadband Single-Cycle Terahertz Pulses with Peak Fields of 300 $\mathrm{kVcm^{-1}}$ from a Metallic Spintronic Emitter. *Appl. Phys. Lett.* **2017**, *110*, 252402.

(2) Kramers, H. A. Some Remarks on the Theory of Absorption and Refraction of X-Rays. *Nature* **1926**, *117*, 774–775.

(3) Kronig, R. d. L. On the Theory of Dispersion of X-Rays. *Josa* **1926**, *12*, 547–557.

(4) Kuzmenko, A. B. Kramers–Kronig Constrained Variational Analysis of Optical Spectra. *Rev. Sci. Instrum* **2005**, *76*, 083108.

(5) Kuzmenko, A. B. Guide to Reffit Software to Fit Optical Spectra. https://reffit.ch/wp-content/uploads/2018/10/Manual.pdf.

(6) Goetzberger, A.; Knobloch, J.; Voss, B. *Crystalline Silicon Solar Cells*; 1998.

(7) Joyce, H. J.; Boland, J. L.; Davies, C. L.; Baig, S. A.; Johnston, M. B. A review of the electrical properties of semiconductor nanowires: insights gained from terahertz conductivity spectroscopy. *Semicond. Sci. Technol* **2016**, *31*, 103003.

(8) D'Angelo, F.; Němec, H.; Parekh, S. H.; Kužel, P.; Bonn, M.; Turchinovich, D. Self-Referenced Ultra-Broadband Transient Terahertz Spectroscopy Using Air-Photonics. *Opt. Express* **2016**, *24*, 10157–10171.

(9) Wehrenfennig, C.; Liu, M.; Snaith, H. J.; Johnston, M. B.; Herz, L. M. Charge-Carrier Dynamics in Vapour-Deposited Films of the Organolead Halide Perovskite $CH_3NH_3PbI_{3-x}Cl_x$. *Energy Environ. Sci.* **2014**, *7*, 2269–2275.

(10) Milot, R. L.; Eperon, G. E.; Snaith, H. J.; Johnston, M. B.; Herz, L. M. Temperature-Dependent Charge-Carrier Dynamics in $CH_3NH_3PbI_3$ Perovskite Thin Films. *Adv. Funct. Mater.* **2015**, *25*, 6218–6227.

(11) La-o Vorakiat, C.; Cheng, L.; Salim, T.; Marcus, R. A.; Michel-Beyerle, M.-E.; Lam, Y. M.; Chia, E. E. Phonon Features in Terahertz Photoconductivity Spectra due to Data Analysis Artifact: A Case Study on Organometallic Halide Perovskites. *Appl. Phys. Lett.* **2017**, *110*, 123901.

(12) Ulatowski, A. M.; Herz, L. M.; Johnston, M. B. Terahertz Conductivity Analysis for Highly Doped Thin-Film Semiconductors. *J. Infrared Millim. Terahertz Waves* **2020**, *41*, 1431–1449.

(13) Wehrenfennig, C.; Liu, M.; Snaith, H. J.; Johnston, M. B.; Herz, L. M. Charge-Carrier Dynamics in Vapour-Deposited Films of the Organolead Halide Perovskite $CH_3NH_3PbI_{3-x}Cl_x$. *Energy Environ. Sci.* **2014**, *7*, 2269–2275.

(14) Xia, C. Q.; Peng, J.; Poncé, S.; Patel, J. B.; Wright, A. D.; Crothers, T. W.; Uller Rothmann, M.; Borchert, J.; Milot, R. L.; Kraus, H., et al. Limits to Electrical Mobility in Lead-Halide Perovskite Semiconductors. *J. Phys. Chem. Lett.* **2021**, *12*, 3607–3617.

(15) Whalley, L. D.; Skelton, J. M.; Frost, J. M.; Walsh, A. Phonon Anharmonicity, Lifetimes, and Thermal Transport in $CH_3NH_3PbI_3$ from Many-Body Perturbation Theory. *Phys. Rev. B* **2016**, *94*, 220301.

(16) Kash, J. A.; Tsang, J. C. Secondary-Emissionstudies of Hot Carrier Relaxation in Polar Semiconductors. *Solid State Electron.* **1988**, *31*, 419–424.

(17) Vonderlinde, D.; Kuhl, J.; Klingenberg, H. Raman-Scattering from Non-Equilibrium LO Phonons with Picosecond Resolution. *Phys. Rev. Lett.* **1980**, *44*, 1505–1508.

(18) Davies, C. L.; Filip, M. R.; Patel, J. B.; Crothers, T. W.; Verdi, C.; Wright, A.; Milot, R. L.; Giustino, F.; Johnston, M. B.; Herz, L. M. Bimolecular Recombination in Methylammonium Lead Triiodide Perovskite Is an Inverse Absorption Process. *Nat. Commun.* **2018**, *9*, 293.

(19) Poncé, S.; Schlipf, M.; Giustino, F. Origin of Low Carrier Mobilities in Halide Perovskites. *ACS Energy Lett.* **2019**, *4*, 456–463.

(20) Marronnier, A.; Roma, G.; Boyer-Richard, S.; Pedesseau, L.; Jancu, J.-M.; Bonnassieux, Y.; Katan, C.; Stoumpos, C. C.; Kanatzidis, M. G.; Even, J. Anharmonicity and Disorder in the Black Phases of Cesium Lead Iodide Used for Stable Inorganic Perovskite Solar Cells. *ACS Nano* **2018**, *12*, 3477.

(21) Whitfield, P.; Herron, N.; Guise, W. E.; Page, K.; Cheng, Y. Q.; Milas, I.; Crawford, M. K. Structures, Phase Transitions and Tricritical Behavior of the Hybrid Perovskite Methyl Ammonium Lead Iodide. *Sci. Rep.* **2016**, *6*, 35685.

(22) Giustino, F. Electron–Phonon Interactions from First Principles. *Rev. Mod. Phys.* **2017**, *89*, 015003.

(23) Schlipf, M.; Poncé, S.; Giustino, F. Carrier Lifetimes and Polaronic Mass Enhancement in the Hybrid Halide Perovskite $CH_3NH_3PbI_3$ from Multiphonon Fröhlich Coupling. *Phys. Rev. Lett.* **2018**, *121*, 086402.

(24) Resta, R. Thomas-Fermi Dielectric Screening in Semiconductors. *Phys. Rev. B* **1977**, *16*, 2717–2722.